Direct Covariance Flux Estimates from Mobile Platforms at Sea*

J. B. EDSON, A. A. HINTON, AND K. E. PRADA

Woods Hole Oceanographic Institution, Woods Hole, Massachusetts

J. E. HARE

Cooperative Institute for Research in Environmental Sciences, University of Colorado, Boulder, Colorado

C. W. FAIRALL

Environmental Technologies Laboratory, NOAA, Boulder, Colorado

(Manuscript received 14 December 1995, in final form 22 April 1997)

ABSTRACT

This paper describes two methods for computing direct covariance fluxes from anemometers mounted on moving platforms at sea. These methods involve the use of either a strapped-down or gyro-stabilized system that are used to compute terms that correct for the 1) instantaneous tilt of the anemometer due to the pitch, roll, and heading variations of the platform; 2) angular velocities at the anemometer due to rotation of the platform about its local coordinate system axes; and 3) translational velocities of the platform with respect to a fixed frame of reference. The paper provides a comparison of fluxes computed with three strapped-down systems from two recent field experiments. These comparisons shows that the direct covariance fluxes are in good agreement with fluxes derived using the bulk aerodynamic method. Additional comparisons between the ship system and the research platform *FLIP* indicate that flow distortion systematically increases the momentum flux by 15%. Evidence suggests that this correction is appropriate for a commonly used class of research vessels. The application of corrections for both motion contamination and flow distortion results in direct covariance flux estimates with an uncertainty of approximately 10%–20%.

1. Introduction

In recent years a great deal of attention has been directed toward air–sea interaction as scientists have begun to study environmental issues by properly treating the ocean and atmosphere as a coupled system. This approach has resulted in a number of air–sea interaction studies, which have united scientists from a variety of disciplines. These studies have also forced researchers to address the problems associated with making high-resolution measurements of turbulence statistics at sea. The problems largely arise from three sources: platform motion, flow distortion, and environmental factors unique to the ocean.

Some of the environmental factors that prove troublesome include the contamination of temperature probes by sea spray (Friehe et al. 1975; Larsen et al. 1993) and mechanical failure induced by a combination of corrosion, wave stress, and unavoidable neglect due to infrequent maintenance. Many of these problems have been overcome by the use of the latest generation of sonic anemometers–thermometers. However, sea-spray contamination of fast-response humidity sensors still plagues marine meteorologists. Dual-wavelength infrared hygrometers have shown some promise in combating this problem in recent field experiments. Unfortunately, these devices often present additional problems (e.g., Fairall and Young 1991), which make the development of a reliable fast-response humidity sensors one of the greatest challenges in marine instrumentation.

Attempts have been made to combat the problems of platform motion and flow distortion by choosing indirect measurement techniques that are less sensitive to their contaminating effects. An example of an indirect measurement is the use of the inertial-dissipation method to infer meteorological fluxes from spectral estimates in the inertial subrange (Fairall and Larsen 1986; Fairall et al. 1990). This method is commonly used on research vessels because the inertial subrange estimates are generally uncontaminated by wave-induced motion. The method has also been shown by Edson et al. (1991) to be less sensitive to flow distortion because it is based

* WHOI Contribution Number 9126.

Corresponding author address: Dr. James B. Edson, AOP&E Dept., Woods Hole Oceanographic Institution, Bigelow 3, Woods Hole, MA 02543.
E-mail: jedson@whoi.edu

on autovariance statistics rather than covariances (see also Anderson 1993; Yelland et al. 1994).

Unfortunately, the inherent limitations of less direct methods can lead to unsatisfactory flux estimates depending on the project's research objectives. For example, the bulk aerodynamic (e.g., Liu et al. 1979; Large and Pond 1981, 1982; Fairall et al. 1996) and inertial dissipation methods have a disadvantage in that they provide only an estimate of the magnitude of the flux. One can assume that the stress is directed along the streamwise velocity component, but recent studies have shown that this is not necessarily the case and that the difference between the two vectors may be an important indicator of larger-scale forcing (Geernaert 1988). Additionally, recent studies by Davidson et al. (1991), Geernaert et al. (1993), and Rieder et al. (1994) have shown that sea-state parameters such as swell and gradients in the surface currents can also influence the direction of the stress vector. Therefore, it is necessary to compute the vector stress using the eddy correlation technique if the objective of the experiment is to understand directional processes.

Second, both indirect methods must rely on additional parameterizations to account for the interaction between the wave field and the surface fluxes. These parameterizations are presently poorly understood and vary widely depending on the oceanic conditions (e.g., open ocean versus coastal zones), such that direct estimates of the fluxes are necessary if we hope to improve these methods. Since these interactions include those associated with surface slicks, wave–current interactions, and temperature stratification, directional stress estimates must be combined with directional wave spectra, current measurements, oceanic and atmospheric stratification parameters, and surfactant concentrations to examine the functional relationship between the wind forcing and wave state. This is clearly a difficult task but one that will become less daunting with the data collected during several field experiments, one of which is briefly discussed in section 6.

Direct covariance (or eddy correlation) measurements generally require an experimental setup around a platform that removes or minimizes the aforementioned effects. One such experimental design is the use of a fixed structure (such as a shallow-water tower) to eliminate platform motion. The sensors are then mounted on low profile masts or booms to move them away from the distorted flow near the platform. This approach was used during the Humidity Exchange over the Sea Main Experiment (HEXMAX), where eddy correlation (or direct covariance) flux estimates were made on a boom extending 17 m upwind of a research platform (Oost et al. 1994). The obvious disadvantage to this approach is that these fixed platforms are relatively scarce and are generally limited to shallow water, and it is often difficult to reduce the flow distortion to satisfactory levels.

Still another approach is to start with a low profile platform, moored buoy (e.g., Dugan et al. 1991; Anctil et al. 1994), or mast, and then correct for platform motion by carefully measuring this motion relative to some reference frame. The systems required to make these measurements generally use a combination of radial and linear accelerometers, compasses, and gyros. These sensors can either be mounted on a stabilized subplatform that has sufficiently slow response to motion or they can be strapped down to the main platform. Signals from both these types of systems are processed in various ways to ultimately produce an estimate of the platform's velocity at the measurement location. Further processing of these signals can be used to estimate the position of the platform relative to the sea surface.

This paper describes our recent efforts to directly measure turbulent fluxes and statistics at sea from mobile platforms using the latter approach. In sections 2–5 we examine the methods used to compute the mean and turbulent meteorological statistics from moving platforms at sea. This involves a detailed description of the methods for obtaining the necessary correction terms using either a strapped-down or gyro-stabilized system. In section 6 we provide a discussion of the results obtained from two strapped-down systems deployed during the High Resolution experiment (Herr et al. 1991). This section describes the system components in some detail and gives examples of the velocity measurements before and after correction to illustrate the effects of motion contamination. The section concludes with a comparison of the eddy correlation derived fluxes with bulk aerodynamic derived estimates.

2. Direct covariance flux systems

The time-averaged flux determined using the eddy correlation technique is regarded as the most direct estimate of the ensemble average flux. In the field, a sonic anemometer is commonly used to provide the three velocity measurements required to compute the vector stress

$$\tau = -\rho[\mathbf{i}\langle u'w'\rangle + \mathbf{j}\langle v'w'\rangle], \tag{1}$$

where ρ is the density of air, the brackets denote a time average, and u', v', and w' are the longitudinal, lateral, and vertical velocity fluctuations about their means. In (1), $-\langle u'w'\rangle$ represents the longitudinal (along wind) component of the stress, and $-\langle v'w'\rangle$ is the lateral component.

The corrected vertical velocity can also be correlated with scalar quantities to compute their vertical flux. In particular, meteorologists are interested in computing the sensible and latent heat fluxes,

$$H = \rho c_p\langle w'\theta'\rangle \tag{2}$$

$$E = \rho L_e\langle w'q'\rangle, \tag{3}$$

respectively, where c_p is the specific heat of air at constant pressure, L_e is the latent heat of evaporation of water, and θ' and q' denote fluctuations in potential

temperature and specific humidity, respectively. These fluxes can then be combined with estimates of the surface stress to compute atmospheric stability parameters.

The obvious problem that arises when estimating these fluxes from a moving platform is that part of the fluctuating velocity is due to platform motion. This motion contamination must therefore be removed before we can compute the fluxes. The contamination arises from three sources: 1) instantaneous tilt of the anemometer due to the pitch, roll, and heading variations of the platform; 2) angular velocities at the anemometer due to rotation of the platform about its local coordinate system axes; and 3) translational velocities of the platform with respect to a fixed frame of reference (Hare et al. 1992).

A variety of approaches have been used to correct wind sensors for platform motion. True inertial navigation systems (Axford 1968; Lenschow and Spyers-Duran 1987) are standard for research aircraft. These systems are expensive and subject to the so-called Schuler oscillation, so simpler techniques have been sought for ships where the platform mean vertical velocity is unambiguously zero. The basic approach that we are using follows that of Fujitani (1981), where the true wind vector (i.e, uncontaminated by motion) can be written as

$$\mathbf{V}_{\text{true}} = \mathbf{T}\mathbf{V}_{\text{obs}} + \boldsymbol{\Omega} \times \mathbf{T}\mathbf{M} + \mathbf{V}_{\text{CM}}, \qquad (4)$$

where $\mathbf{V}_{\text{true}}$ is the desired wind velocity vector in the reference coordinate system, $\mathbf{V}_{\text{obs}}$ is the measured wind velocity vector in the platform frame of reference, $\mathbf{T}$ is the coordinate transformation matrix for a rotation of the platform frame coordinate system to the reference coordinates, $\boldsymbol{\Omega}$ is the angular velocity vector of the platform coordinate system, $\mathbf{M}$ is the position vector of the wind sensor with respect to the center of gravity, and $\mathbf{V}_{\text{CM}}$ is the translational velocity vector at the center of motion of the platform with respect to a fixed coordinate system.

If the motion measurement system is not located at the center of motion, then an additional correction term arises due to angular velocities that are sensed at that location as translational velocities by the accelerometers (Fujitani 1985). This term is incorporated in (4) as

$$\mathbf{V}_{\text{true}} = \mathbf{T}\mathbf{V}_{\text{obs}} + \boldsymbol{\Omega} \times \mathbf{T}(\mathbf{M} - \mathbf{S}) + \mathbf{V}_{\text{mot}}, \qquad (5)$$

where $\mathbf{S}$ is the vector distance from the motion system to the center of motion of the platform and $\mathbf{V}_{\text{mot}}$ now includes the additional translational velocities. Fortunately, $\mathbf{M} - \mathbf{S}$ is just the position vector of the wind sensor with respect to the motion package. Therefore, one does not need to know the exact location of the center of motion, which is often difficult to identify.

3. Angles and angular rates

To use (5), we need three angular variables describing the platform's orientation in the fixed frame and the angular velocity vector describing the time rate of change of its orientation. Several different angular coordinate systems are available (Goldstein 1965), but roll ϕ, pitch θ, and yaw Ψ are most often used because they are the variables output from common doubly gimbaled gyro-stabilized systems. In the sections that follow, we will describe two common approaches to compute these variables from moving platforms.

a. Gyro-stabilized systems

Gyro-stabilized systems provide the user with pitch, roll, and yaw angles that describe the ship's orientation in the fixed frame. These angles can be used directly in the total rotational coordinate transformation matrix that we define as

$$\begin{aligned}
&\mathbf{T}(\phi, \theta, \Psi) \\
&\quad = A(\Psi)A(\theta)A(\phi) \\
&\quad = \begin{bmatrix} \cos(\Psi) & \sin(\Psi) & 0 \\ -\sin(\Psi) & \cos(\Psi) & 0 \\ 0 & 0 & 1 \end{bmatrix} \begin{bmatrix} \cos(\theta) & 0 & \sin(\theta) \\ 0 & 1 & 0 \\ -\sin(\theta) & 0 & \cos(\theta) \end{bmatrix} \begin{bmatrix} 1 & 0 & 0 \\ 0 & \cos(\phi) & -\sin(\phi) \\ 0 & \sin(\phi) & \cos(\phi) \end{bmatrix}, \\
&\quad = \begin{bmatrix} \cos(\Psi)\cos(\theta) & \sin(\Psi)\cos(\phi) + \cos(\Psi)\sin(\theta)\sin(\phi) & -\sin(\Psi)\sin(\phi) + \cos(\Psi)\sin(\theta)\cos(\phi) \\ -\sin(\Psi)\cos(\theta) & \cos(\Psi)\cos(\phi) - \sin(\Psi)\sin(\theta)\sin(\phi) & -\sin(\theta)\cos(\phi)\sin(\Psi) - \sin(\phi)\cos(\Psi) \\ -\sin(\theta) & \cos(\theta)\sin(\phi) & \cos(\theta)\cos(\phi) \end{bmatrix}, \qquad (6)
\end{aligned}$$

where the sign convention here is based on a right-handed (x, y, z) coordinate system with x positive forward (to bow), y positive to port, z positive upward, Ψ positive for the ship's bow yawed clockwise from north, ϕ positive for the port side rolled up, and θ positive for the bow pitched down. Note that ϕ and θ are right-handed rotations, but to conform to the normal convention for heading, we have used a left-handed defi-

nition for Ψ. This definition allows us to directly use the platform's compass in the transformation matrix.

Equation (6) represents the coordinate system transform for a combination of the three separate rotations of the platform coordinate frame about the three axes of our frame of reference (i.e., the earth). Note that this total coordinate transformation matrix is dependent on the order of the three separate rotations. However, for small roll and pitch angles such as those encountered on a large research vessel or discus buoy in the ocean environment (perhaps $\pm 10°$), the error due to the order of rotation is negligible. On smaller vessels such as the towed catamaran described in section 6, the errors associated with the order of rotation are minimized by the 3, 2, 1 rotation used in (6). Additionally, these errors remain small simply because the catamaran cannot be operated in high sea states, such that the angles rarely exceed $\pm 10°$.

The three angular rates can be computed from the time derivatives of the orientation angles. Unfortunately, only yaw is measured in the fixed frame, pitch is measured in a yawed frame, and roll is measured in a pitched and yawed frame. Thus, the time derivatives of these angles must be rotated to create a fixed frame angular rate pseudovector given by

$$\boldsymbol{\Omega} = \begin{bmatrix} 0 \\ 0 \\ -\dot{\Psi} \end{bmatrix} + A(\Psi)\begin{bmatrix} 0 \\ \dot{\theta} \\ 0 \end{bmatrix} + A(\Psi)A(\theta)\begin{bmatrix} \dot{\phi} \\ 0 \\ 0 \end{bmatrix}$$

$$= \begin{pmatrix} \dot{\phi}\cos(\Psi)\cos(\theta) + \dot{\theta}\sin\Psi \\ \dot{\theta}\cos(\Psi) - \dot{\phi}\sin(\Psi)\cos(\theta) \\ -\dot{\Psi} - \dot{\phi}\sin(\theta) \end{pmatrix}, \quad (7)$$

where the overdot denotes a time derivative. This vector can then be used in either (4) or (5) to compute the required angular velocities.

b. Strapped-down systems

As an alternative to gyro-stabilized pitch and roll sensors, it is also common practice to use angular rate sensors that measure the rate of angular rotation about the three axes in the platform frame. These systems are often referred to as strapped-down systems because the motion package is firmly attached to the platform frame. In such systems, the angular rate vector is given by

$$\boldsymbol{\Omega}_{\text{obs}} = \begin{pmatrix} \dot{\phi}_{\text{obs}} \\ \dot{\theta}_{\text{obs}} \\ -\dot{\Psi}_{\text{obs}} \end{pmatrix}, \quad (8)$$

where the subscript obs again denotes measurements made in the platform's frame of reference. We remind the reader that the yaw rate is defined positive for a left-handed rotation. The negative sign in front of the yaw rate is therefore required to compute the angular velocities in our otherwise right-handed coordinate system. We feel that the small amount of confusion that this introduces is more than offset by the ease in which the platform's heading is introduced into the corrections. This vector can be related to the fixed frame angular rate through

$$\boldsymbol{\Omega} = \mathbf{T}\boldsymbol{\Omega}_{\text{obs}}. \quad (9)$$

This relationship allows one to rewrite (5) using our direct measurements of angular rate in the platform frame as

$$\mathbf{U}_{\text{true}} = \mathbf{T}(\mathbf{U}_{\text{obs}} + \boldsymbol{\Omega}_{\text{obs}} \times \mathbf{R}) + \mathbf{V}_{\text{mot}}, \quad (10)$$

where $\mathbf{R}$ is the position vector of the wind sensor with respect to the motion package.

The difficulty then is to approximate ϕ, θ, and Ψ from the strapped-down angular rate sensors. The general approach is to use (6) and (7) in (9) to obtain an expression for the time derivative of these angles in terms of the measured angular rates given by

$$A(\Psi)A(\theta)A(\phi)\begin{bmatrix} \dot{\phi}_{\text{obs}} \\ \dot{\theta}_{\text{obs}} \\ -\dot{\Psi}_{\text{obs}} \end{bmatrix}$$

$$= \begin{bmatrix} 0 \\ 0 \\ -\dot{\Psi} \end{bmatrix} + A(\Psi)\begin{bmatrix} 0 \\ \dot{\theta} \\ 0 \end{bmatrix} + A(\Psi)A(\theta)\begin{bmatrix} \dot{\phi} \\ 0 \\ 0 \end{bmatrix}. \quad (11)$$

Using the coordinate system defined above, a few algebraic manipulations result in the following expression:

$$\begin{bmatrix} \dot{\phi} \\ \dot{\theta} \\ -\dot{\Psi} \end{bmatrix} = \begin{pmatrix} \dot{\phi}_{\text{obs}} + [-\dot{\Psi}_{\text{obs}}\cos(\phi) + \dot{\theta}_{\text{obs}}\sin(\phi)]\tan(\theta) \\ \dot{\theta}_{\text{obs}}\cos(\phi) + \dot{\Psi}_{\text{obs}}\sin(\phi) \\ [-\dot{\Psi}_{\text{obs}}\cos(\phi) + \dot{\theta}_{\text{obs}}\sin(\phi)]/\cos(\theta) \end{pmatrix}, \quad (12)$$

which we can rewrite using small angle approximations as

$$\begin{bmatrix} \dot{\phi} \\ \dot{\theta} \\ -\dot{\Psi} \end{bmatrix} \approx \begin{pmatrix} \dot{\phi}_{\text{obs}} - \dot{\Psi}_{\text{obs}}\theta \\ \dot{\theta}_{\text{obs}} + \dot{\Psi}_{\text{obs}}\phi \\ -\dot{\Psi}_{\text{obs}} + \dot{\theta}_{\text{obs}}\phi \end{pmatrix}. \quad (13)$$

In principle, (12) could be integrated by updating this matrix with successive approximation of ϕ and θ as one stepped through the measurements. In practice, problems often arise with this approach due to the drift found in angular rate sensors. Therefore, the angles are generally found by high-pass filtering the angles that are computed by integration of (12) or (13) and then adding these results to low-pass filtered reference angles. This is the approach taken by Fairall et al. (1997) and Thwaites et al. (1995).

c. Complementary filtering

The Woods Hole Oceanographic Institution (WHOI) system uses a slightly simpler approach based on complementary filtering. In a strapped-down system, the measured accelerometer output is a combination of the gravitational component due to the pitching and rolling of the platform (i.e., due to tilting of the system) plus the accelerations arising from the motion of the platform along the accelerometer axes

$$\begin{pmatrix} \ddot{x}_{\text{obs}} \\ \ddot{y}_{\text{obs}} \\ \ddot{z}_{\text{obs}} \end{pmatrix} = \begin{pmatrix} \ddot{x} \\ \ddot{y} \\ \ddot{z} \end{pmatrix} + \begin{pmatrix} -g \sin(\theta) \\ g \sin(\phi) \cos(\theta) \\ g \cos(\phi) \cos(\theta) \end{pmatrix}, \tag{14}$$

where the double dots denote second derivatives of the position vector $\mathbf{X} = (x, y, z)$, and g is the gravitational acceleration.

The second term on the right-hand side of (14) represents the tilt-induced acceleration. These tilt-induced accelerations will eventually have to be removed before we integrate our accelerometers to compute the platform velocities as described in section 4. However, we can use these measured accelerations and angular rates to approximate the desired angles using complementary filtering.

We can easily illustrate this technique using Laplace transform notation, where we estimate ϕ, θ, and Ψ by applying filters to our signals to obtain

$$\phi \approx \frac{1}{\tau s + 1} \frac{\ddot{y}_{\text{obs}}}{g} + \frac{\tau s}{\tau s + 1} \phi_{\text{obs}} \tag{15}$$

$$\theta \approx \frac{1}{\tau s + 1} \frac{\ddot{x}_{\text{obs}}}{g} + \frac{\tau s}{\tau s + 1} \theta_{\text{obs}} \tag{16}$$

and

$$\Psi \approx \frac{1}{\tau s + 1} \Psi_{\text{slow}} + \frac{\tau s}{\tau s + 1} \Psi_{\text{obs}}, \tag{17}$$

where s represents the differentiation operator such that $\dot{\phi}_{\text{obs}} = s\phi_{\text{obs}}$, τ is a time constant, Ψ_{slow} represents the compass output, and we have again assumed that these angles are small in (15) and (16). The first term on the right-hand side is the low-frequency tilt reference from the accelerometers as follows from (14). The second term on the right-hand side represents a high-pass filter [i.e., $\tau s/(\tau s + 1)$] that integrates the angular rate sensors to provide the wave-induced angular motions. By filtering the signals in this way we do not introduce any time delays, that is, the process is an all-pass filter that removes the unwanted drift in the rate gyros while retaining the low-frequency tilt reference.

In practice, these expression can be rewritten in the form

$$\phi \approx \frac{1}{\tau s + 1} \left[\tau \dot{\phi}_{\text{obs}} + \frac{\ddot{y}_{\text{obs}}}{g} \right], \tag{18}$$

so that we can compute the angles by performing an FFT on the bracketed expressions, applying the above first-order Butterworth filter in frequency space, and then performing an inverse FFT to obtain the time series of ϕ, θ, and Ψ. Alternatively, we have computed the angles using a digital filter on the time series such that

$$\begin{aligned} \phi(t) \approx\ & B_1 \left[\tau_c \dot{\phi}(t)_{\text{obs}} + \frac{\ddot{y}(t)_{\text{obs}}}{g} \right] \\ & + B_0 \left[\tau_c \dot{\phi}(t - \Delta t)_{\text{obs}} + \frac{\ddot{y}(t - \Delta t)_{\text{obs}}}{g} \right] \\ & + A_1 \phi(t - \Delta t), \end{aligned} \tag{19}$$

where Δt is the time step between samples, τ_c is the filter time constant given by

$$\tau_c = \frac{\Delta t}{2\omega_c}, \tag{20}$$

where ω_c is the prewarped frequency

$$\omega_c = \tan\left(\frac{\Delta t}{2\tau}\right) \tag{21}$$

and the filter coefficients are given by Hamming (1977) as

$$A_1 = \frac{1 - \omega_c}{1 + \omega_c}, \qquad B_0 = B_1 = \frac{\omega_c}{1 + \omega_c}. \tag{22}$$

While both techniques give essentially the same results, the latter approach may turn out to be more attractive since one could design an analog system that filters the combined signals before they reach the data acquisition computer. This would allow the angles to be computed in real time, without any loss of data (after a short spinup period) and less computational processing. The digital filter approach is used to compute the flux estimates presented in section 6.

The choice of the time constant τ is dependent on how the platform responds to the wave field. During the High Resolution Main Experiment, our spectra showed that the peak in the accelerometer spectra generally occurred around $f_n = 0.2$–0.25 Hz, that is, the platforms were responding strongly to 4–5-s waves. Since the accelerometers are sensing both platform and tilt-induced accelerations about this maximum, it is necessary to use a much longer time constant to obtain the low-frequency tilts. In practice, we have found that a value of τ equal to $5/(2\pi f_m)$ provides a smooth transition between the spectral components as shown in Fig. 1.

4. Translational velocities

Historically, instruments that measure absolute velocities have not been available (differential GPS may soon change this). As a result, velocities are usually computed by integrating measurements of platform acceleration after removal of the tilt-induced components discussed in section 3c. The removal of all traces of the

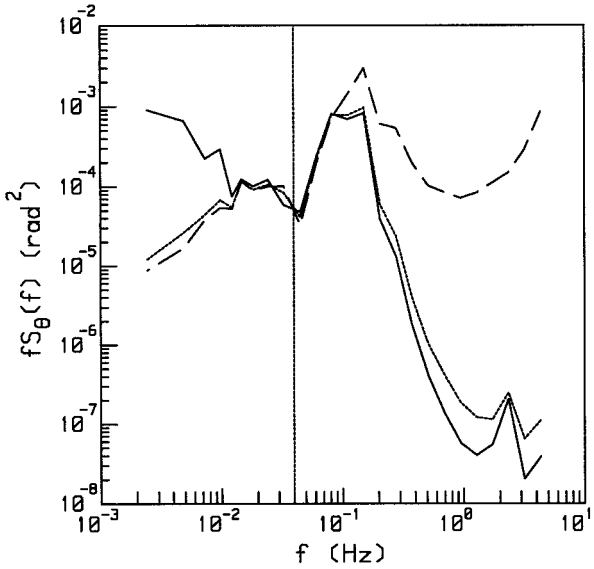

FIG. 1. The variance spectra of our angular estimates of θ. The broken line is computed from $-x/g$, the solid line is computed from a time series of the integrated rate sensor, and the dotted line is computed using complementary filtering. The vertical line in the figure shows the location of our cutoff frequency $f_m/5$.

tilt-induced components in our measured accelerations is a difficult task. Additionally, ship maneuvers require accurate measurements of the low-frequency translational velocity that can be difficult to obtain from the integrated accelerations. Therefore, we again rely on filtering to provide us with the high- and low-frequency translational velocity components.

To illustrate this process, we rewrite the translational velocity as

$$\mathbf{V}_{\text{mot}} = \mathbf{V}_{\text{lp}} + \mathbf{V}_{\text{hp}}, \tag{23}$$

where we have divided the translational velocities into low-pass (lp) and high-pass (hp) components. In the strapped-down systems, the high-pass components are computed by rotating the accelerations into the fixed frame using the transformation matrix $\mathbf{T}(\phi, \theta, \psi)$, subtracting the gravity vector, high-pass filtering and integrating the remainder, and then high-pass filtering the resultant velocities,

$$\mathbf{V}(t)_{\text{hp}} = \text{Hp}\left[\int [\text{Hp}(\mathbf{T}\ddot{\mathbf{x}}(t)_{\text{obs}} + \mathbf{g})]\, dt\right], \tag{24}$$

where Hp represents a high-pass filter operator and $\mathbf{g} = (0, 0, -g)$. The same expression applies for the gyro-stabilized velocities except that the gyro-stabilized accelerometers need only be rotated to account for any change in heading before subtraction of gravity. This high-passed component represents the wave-induced motions of the anemometer where we typically use a time constant of 2 min for the filter.

The low-pass components are computed only for the horizontal velocities (i.e., we assume the platform does not leave the ocean surface) using either GPS or a current meter that measures the platform speed relative to water. The combination of the high-pass and low-pass signals results in a value of $\mathbf{V}_{\text{mot}}$ that describes the mean velocity platform relative to earth (measured with a GPS system) or relative to water (measured with a current meter) plus the fluctuating velocity components computed from our accelerometers. The method used to compute the low-frequency component depends on whether we are using real-time or postprocessing of the data as described below.

5. Data processing

For real-time processing we use simple exponential time filters and compute fluxes in 10-min blocks. These simple filters introduce a time lag that must be taken into account before the high-pass platform velocities are added to transformed velocities in (10). The mean translational motion of the platform is computed over the 10-min period and then added to the otherwise corrected velocities at the end of the averaging period (i.e., the low-pass time constant is 10 min). The averages, variances, and covariances are then computed and displayed at the end of each averaging period. This allows us to check the system performance during the cruise.

A flowchart for the postprocessing procedure is given in Fig. 2, which is intended to summarize the process described above. In this procedure we first remove any mean in our angular rate time series when the angles are found from complementary filtering. This step helps offset the gentle roll-off of our first-order Butterworth filters and gives us more flexibility in choosing the cutoff frequency $1/\tau$. We then use time-symmetric high-pass filters to avoid time lags in our translational velocities and apply the low-pass filtered GPS or current meter data at every time step. In this instance, the low-pass time constant is chosen to compliment the high-pass filter.

The relative velocity components obtained from our current meters are rotated by the transformation matrix to give the north and west components. When these are added from the north and west components of the wind speed relative to the platform we obtain the wind velocity relative to the water,

$$\mathbf{U}_{\text{true}}^{\text{water}} = \mathbf{T}(\mathbf{U}_{\text{obs}} + \boldsymbol{\Omega}_{\text{obs}} \times \mathbf{R}) + \mathbf{V}_{\text{hp}} + \text{Lp}[\mathbf{T}\mathbf{V}_o], \tag{25}$$

where $\mathbf{V}_o$ is the platform velocity relative to water and Lp represents a low-pass filter operator. Equation (25) provides us with the relative velocity used in our bulk flux algorithm. The GPS system is used to directly compute the north and west components of the ship speed relative to earth. These are then used to compute the north and west components of the wind velocity relative to earth:

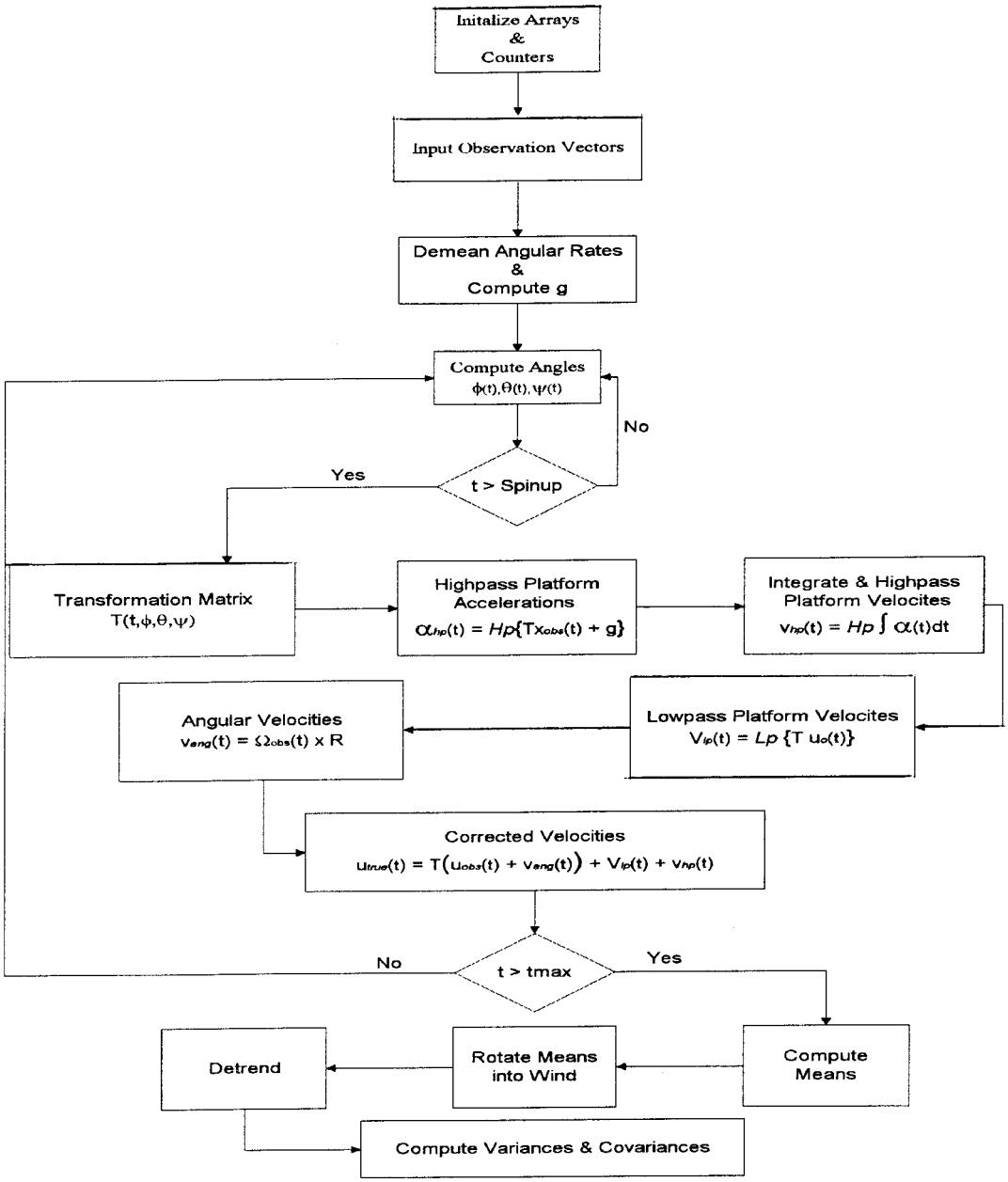

FIG. 2. A flowchart of the method used to postprocess the data. Spinup represents the time given to the complementary filters to provide the proper angles, while t_{max} represents the record length.

$$\mathbf{U}_{\text{true}}^{\text{earth}} = \mathbf{T}(\mathbf{U}_{\text{obs}} + \boldsymbol{\Omega}_{\text{obs}} \times \mathbf{R}) + \mathbf{V}_{\text{hp}} + \text{Lp}[\mathbf{V}_{\text{GPS}}]. \tag{26}$$

The wind components relative to earth are then used to compute the wind direction by taking the four quadrant arctangents of the negative north (i.e., south) and west components to determine where the wind is coming from in earth coordinates. The velocity of the ship relative to water and the ship relative to earth are then combined to compute the actual value of the near-surface current.

The velocities in these two coordinates systems are generally rotated into the streamwise wind (i.e., $\overline{V} = \overline{W} = 0$ after rotation) and linearly detrended by removing a least squares fit to the rotated velocities. The fluxes are then computed in the along-wind and cross-wind directions. However, the north and west components of the fluxes are sometimes computed, particularly when we want to map the flux field over a survey cruise. For example, this approach would be desirable if we wished to examine the curl of the stress vector to study upwelling.

Finally, it is worth noting that our stress values tend

to be invalidated by drastic platform maneuvers, which add low-frequency noise to the flux cospectra. In fact, our real-time stress estimates tend to be invalidated by even modest platform maneuvers because the low-pass filter in the real-time processing is essentially a 10-min block average. Therefore, the preferred mode of operation is to take measurements under way at a constant speed and heading whenever possible. In postprocessing the data, however, our algorithms are able to correct for heading changes. The data given in section 6 are taken from the postprocessed flux estimates, where the mean relative wind direction was limited to $\pm 90°$ from the bow.

6. Discussion of results

In the discussion that follows, we will focus on measurements made using the WHOI flux system during the High Resolution and Marine Boundary Layers (MBLs) experiments. Results from the system deployed by NOAA's Environmental Technology Laboratory can be found in Fairall et al. (1997). The High Resolution program is an Office of Naval Research (ONR)-sponsored Accelerated Research Initiative that was designed to investigate surface signatures in radar backscatter measurements in and around the Gulf Stream. This region was selected because the gradients associated with sea surface temperature and current fronts often give rise to roughness contrasts that cause the features seen in remotely sensed images. In these regions it is especially important to compute the fluxes in a frame of reference moving with the ocean surface. This is because the momentum flux, at least in a bulk sense, is proportional to the relative difference between the wind and current velocities.

The MBL experiment was another ONR-sponsored research program that took place off the California coast. The experiment was conducted from research vessels, an aircraft, and the research platform *FLIP*. The R/P *FLIP* is a 110-m-long spar buoy that provides a relatively stable platform for ocean-going research (particularly when compared with research vessels). The meteorological measurements made aboard the *FLIP* used a low profile mast erected off its port boom. Comparisons between the *FLIP* data and flux estimates taken aboard the research vessel are used to investigate the influence of flow distortion on our measurements.

a. The WHOI direct covariance flux system

The WHOI Direct Covariance Flux System (DCFS) has been deployed in two recent field experiments on three platforms. Two ship-based systems have been on bow masts aboard the R/V *Columbus Iselin* during the High Resolution Main Experiment and from the R/V *Wecoma* during the MBL experiment. Additionally, a DCFS was deployed aboard the laser slope gauge, acoustic Doppler current profiler, Attitude measurement unit, sonic anemometer (*LADAS*) catamaran that was towed from the R/V *Columbus Iselin*, as shown in Fig. 3. The *LADAS* has been developed to allow us to study a wide range of microscale and mesoscale processes within the oceanic and atmospheric boundary layers by integrating several systems on a single platform. The catamaran is remotely ''flown'' outside of the wake of the research vessel, with power and signals going to and from the vessel by way of the towing cable. The platform is designed to collocate the probes as much as possible so as to study cause and effect on very fine spatial and temporal scales, while making the platform itself much less obtrusive to the environment than previous ocean-going platforms. The catamaran has additional advantages over buoys in that it is highly mobile and is not limited by power consumption restraints.

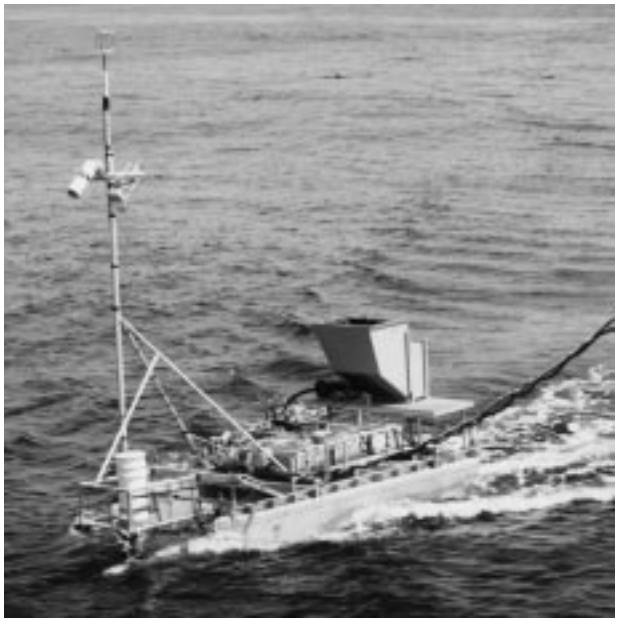

FIG. 3. The R/P *LADAS* catamaran. The sonic anemometer is mounted on the mast above the starboard pontoon. The Honeywell AMU was located in one of the splash-proof containers near the center of the catamaran.

The 1993 High Resolution Main Experiment was conducted off Cape Hatteras in and around the Gulf Stream. The primary objective of these experiments was to examine the relationship between microwave remote sensing, meteorological forcing, and oceanic surface processes. In this regard, the scientific team instrumenting the R/P *LADAS* was most interested in making accurate measurements of the meteorological forcing through wind stress and the short-wave component of the wave spectrum, which is the primary source for microwave backscatter from the ocean surface. The system used to measure the short-wave spectra is described in detail by Bock and Hara (1995).

The meteorological package aboard all three platforms consisted of a Solent three-axis sonic anemom-

FIG. 4. The Direct Covariance Flux System used aboard the R/Vs *Iselin* and *Wecoma.* The anemometer is mounted directly above the metal canister that houses the MotionPAK AMU sensors. The sensor mounted horizontally below the canister is an Ophir infrared hygrometer. The antenna for the GPS receiver integrated into the system is visible on the horizontal crosspiece.

eter–thermometer and a Väisälä relative humidity–temperature sensor with a radiation shield. The sonic anemometer and Väisälä units were deployed 5.6, 11.5, and 11.3 m above the mean sea surface on the R/P *LADAS*, R/V *Iselin*, and R/V *Wecoma*, respectively. The ship-based systems also included an Ophir infrared hygrometer in order to make direct estimates of the latent heat flux, as shown in Fig. 4.

The R/P *LADAS* used a Honeywell MK 50 Attitude Measurement Unit (AMU) to provide the three axes angular rates and linear accelerations needed to correct the various measurement systems onboard. The AMU is strapped down near the center of mass of the catamaran, which was 5.3 m away from the sonic sampling volume. The R/P *LADAS* computed the mean velocity relative to water using a SimTronix UCM 40 three-axis current meter provided by Johns Hopkins Applied Physics Laboratory. The current meter also contained a compass to provide heading and a temperature probe for the near sea surface temperature. The current meter was deployed approximately 1 m forward and between the catamaran's pontoons at a depth of 1 m.

The ship-based DCFS used the three-axis accelerometers and rate sensors provided by a Systron Donner MotionPAK. The MotionPAK was mounted directly beneath the sonic anemometer package, which decreased the distance between the sensors and the sonic sampling volume to $|\mathbf{R}| \approx 1$ m in (10), as shown in Fig. 4. The

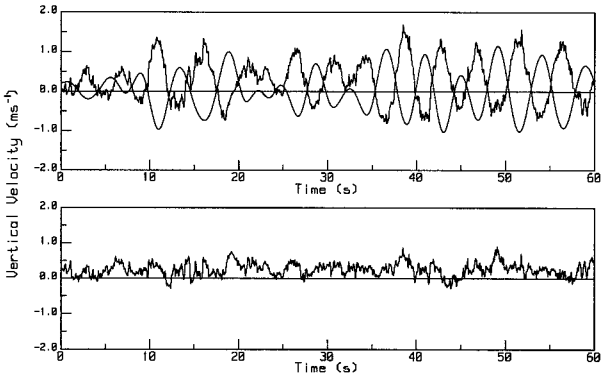

FIG. 5. The top panel shows a time series of the measured sonic vertical velocity (solid line) with the high-passed vertical velocity correction $W_{hp}(t)$. The bottom panel shows the true vertical velocity computed from Eq. (10).

R/V *Iselin* used the ship's gyrocompass to obtain heading, while the R/V *Wecoma* system incorporated a Precision Navigation compass. A hull-mounted ADCP provided the relative velocity for both ships using the uppermost bins of the ADCP data. A temperature probe was dragged off the side of the ships to provide the DCFS with a continuous record of near-surface temperature.

b. Platform contamination

A segment of a uncorrected sonic vertical velocity time series taken from the R/V *Iselin* is shown in Fig. 5 along with the computed velocity correction. Obviously most of the fluctuating signal seen by the anemometer in this time series is platform motion. This figure also indicated that a mean vertical velocity remains even after correction. The residual tilt varies from approximately 3° to 5° for relative wind directions from 0° (i.e., toward the bow) to ±90° (from port or starboard). The residual tilt on the R/P *LADAS* is always less than 1° for the relative wind directions used in this analysis. We believe that the larger residual tilt is due to flow distortion by the vessel's superstructure and provide evidence for this in section 5d.

The corresponding vertical velocity spectra are shown in Fig. 6, where the motion is apparent as a spike at about 0.25 Hz in the uncorrected spectrum. This figure shows that this spike is effectively removed after the correction procedure has been applied. The low-frequency changes in the velocity spectra are due to the instantaneous tilt corrections, which add components of the other two velocity measurements, as well as the low-frequency translational motion of the platform (only the mean was removed from the uncorrected time series).

The effect of motion contamination in our flux estimates can be examined in detail using the cospectral equivalent of (1). The cospectral estimates of the stress components are shown in Figs. 7 and 8. The uncorrected components are clearly contaminated by a spike in the

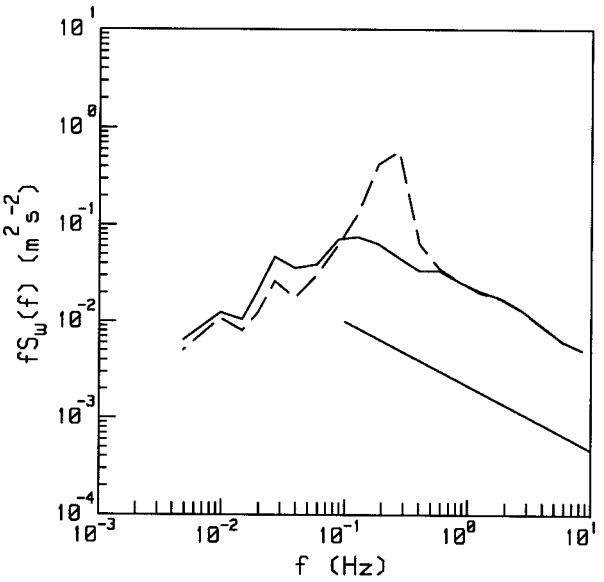

FIG. 6. The measured (broken line) and corrected (solid line) vertical velocity power spectra. The spectra are computed from the average of three 3-min time series within a 10-min record. The straight line in the figure represents the expected $-2/3$ slope in the inertial subrange.

cospectra occurring at the frequency f_m. This spike dominates the signal and results in a positive values of the longitudinal momentum fluxes when we integrate under the curve. However, when we remove the platform contamination from our signals we obtain cospectra that agree well with empirical predictions. An example of this is shown in Fig. 9 where we have plotted the corrected a *uw* cospectrum versus the empirical formula determined by Kaimal et al. (1972).

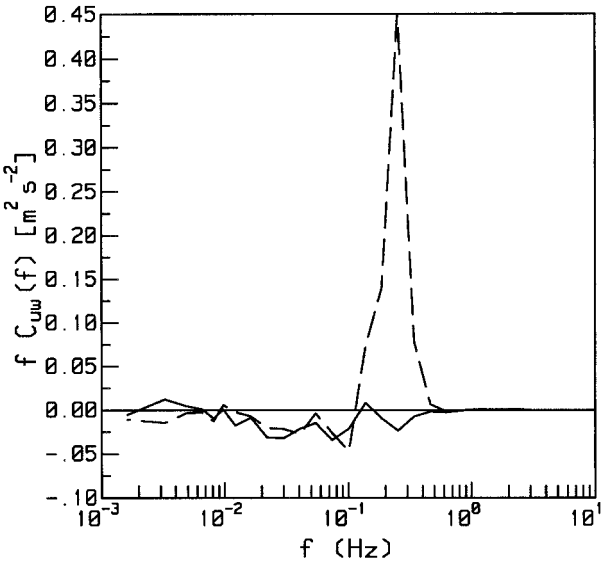

FIG. 7. The uncorrected (broken line) and corrected (solid line) covariance spectra for the longitudinal component of the momentum flux.

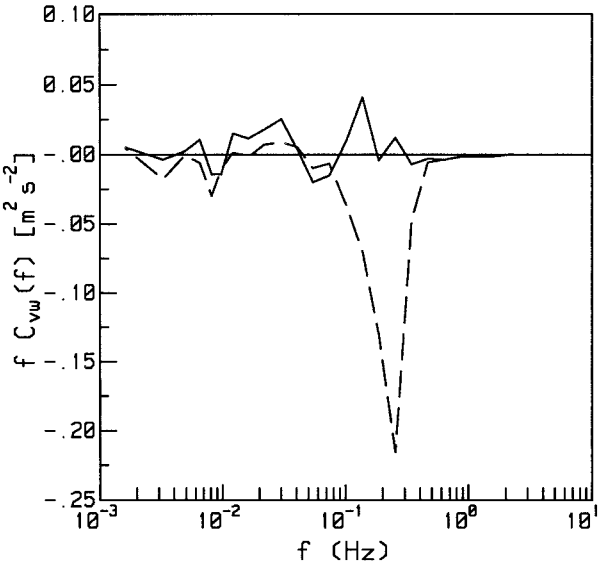

FIG. 8. The uncorrected (broken line) and corrected (solid line) covariance spectra for the lateral component of the momentum flux.

c. Flux comparisons

The mean instrumentation was used to compute the fluxes using the bulk aerodynamic method, which served as a useful means to compare our flux estimates. The bulk aerodynamic flux estimates are determined using an algorithm given in Fairall et al. (1996) that combines the surface roughness parameterization from Smith (1988) with the heat flux parameterizations described by Liu et al. (1979). In Figs. 10–13, the uncorrected and corrected covariance stress estimates are

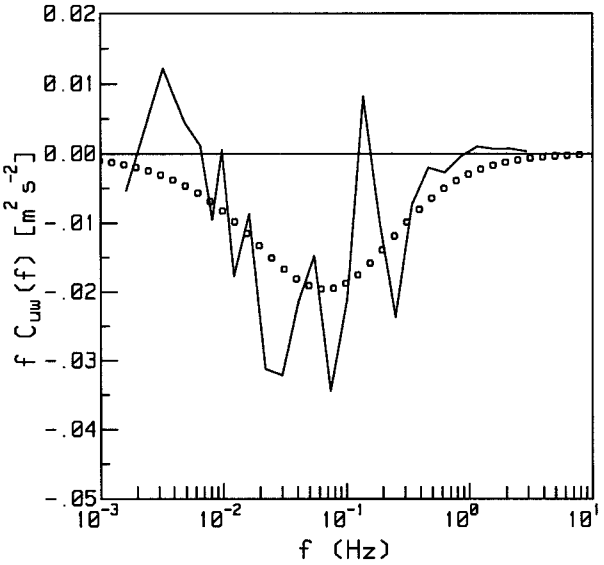

FIG. 9. The corrected (solid line) covariance spectra for the longitudinal component of the momentum flux plotted with a parameterization of this component (dotted line) reported in Kaimal et al. (1972).

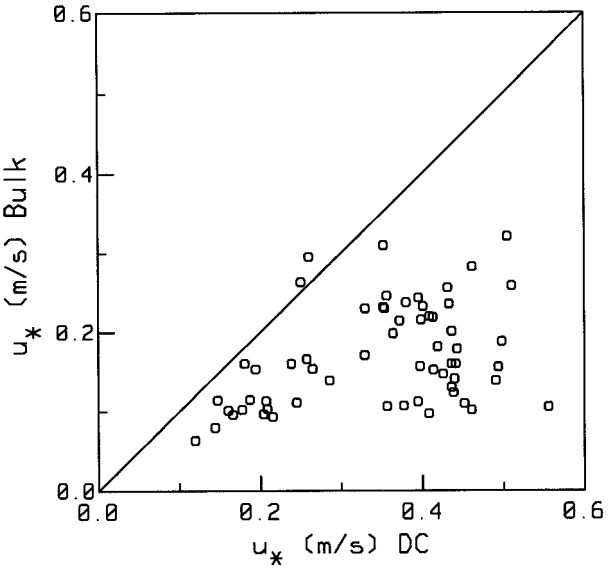

FIG. 10. A comparison of the uncorrected friction velocity estimates from the R/P *LADAS* computed from Eq. (27) vs our bulk aerodynamic estimates. The fluxes represent 30-min averages computed from three 10-min estimates.

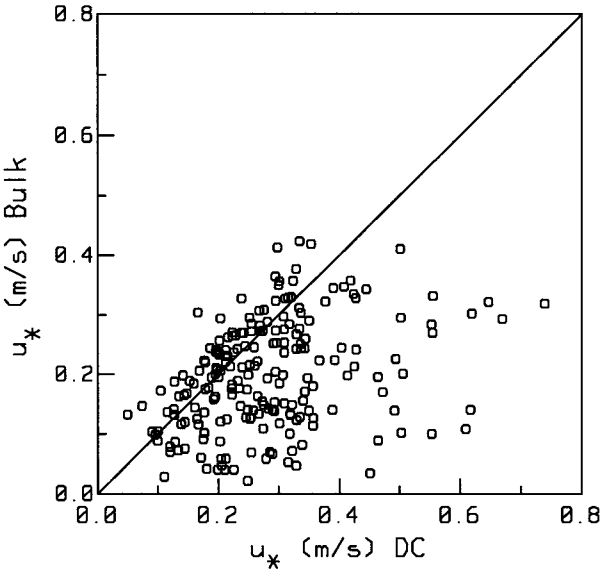

FIG. 12. A comparison of the uncorrected friction velocity estimates from the R/V *Iselin* computed from Eq. (27) vs our bulk aerodynamic estimates. The fluxes represent 30-min averages computed from three 10-min estimates.

compared against the bulk aerodynamic method where the velocity scaling parameter (i.e, the friction velocity) is defined as

$$u_* = [\langle u'w' \rangle^2 + \langle v'w' \rangle^2]^{1/4}. \quad (27)$$

Figures 10 and 11 show comparisons of the covariances computed before and after correction, respectively, using the strap-down system on the R/P *LADAS*, while Figs. 12 and 13 give the same comparisons for the R/V *Iselin.* Clearly, the agreement between the two methods is dramatically improved through correction, where the platform motion tends to cause an increase in the correlation between the signals that leads to an overestimation of the flux. There is very good agreement between the direct covariance and bulk estimates from the R/P *LADAS.* However, there appears to be some additional scatter and bias in the R/V *Iselin* comparison.

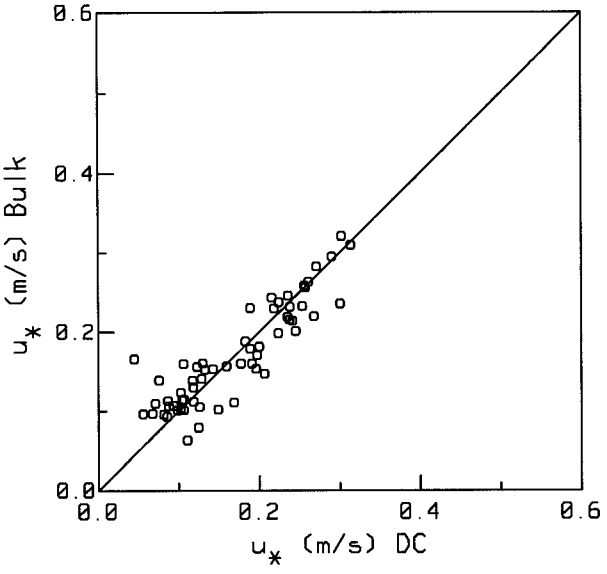

FIG. 11. A comparison of the corrected friction velocity estimates from the R/P *LADAS* computed from Eq. (27) vs our bulk aerodynamic estimates. The fluxes represent 30-min averages computed from three 10-min estimates.

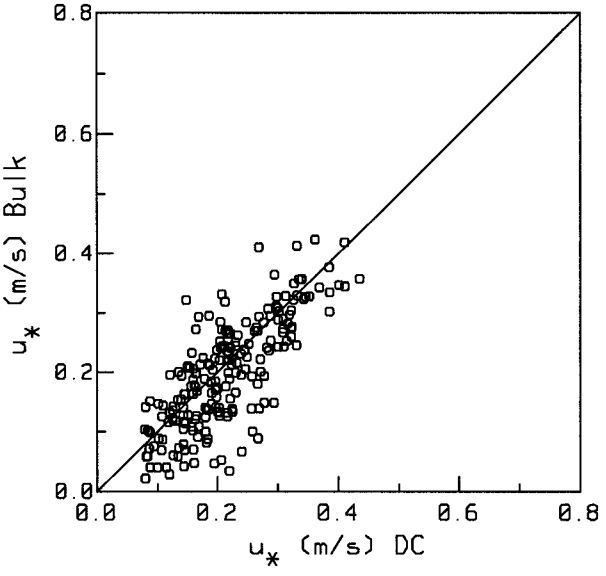

FIG. 13. A comparison of the corrected friction velocity estimates from the R/V *Iselin* computed from Eq. (27) vs our bulk aerodynamic estimates. The fluxes represent 30-min averages computed from three 10-min estimates.

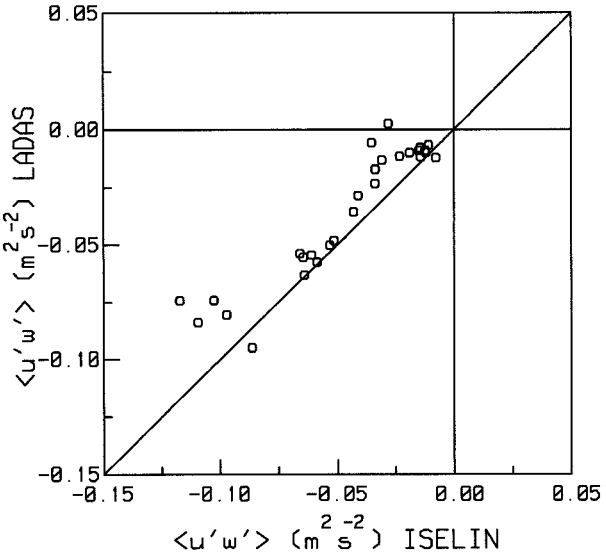

FIG. 14. A comparison of measurements of the longitudinal component $\langle u'w' \rangle$ of the momentum flux taken from the R/V *Iselin* and R/P *LADAS*. The data represent 30-min averages where there is at least 20 min of overlap between the estimates.

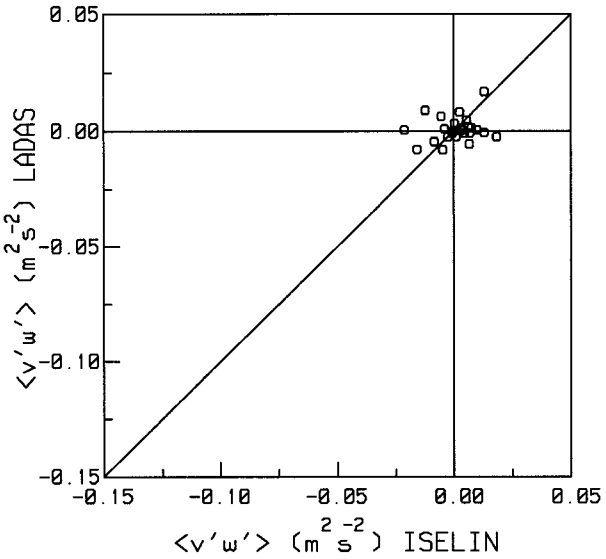

FIG. 15. A comparison of measurements of the lateral component $\langle v'w' \rangle$ of the momentum flux taken from the R/V *Iselin* and R/P *LADAS*. The data represent 30-min averages where there is at least 20 min of overlap between the estimates.

This bias is also evident in the comparison of the direct-covariance stress components computed from the R/P *LADAS* and R/V *Iselin*. These fluxes were computed by averaging together three 10-min estimates. We expect our 10-min averages to miss some of the turbulent flux that would result in an underestimation of the flux, particularly for the measurements under the low winds from the R/P *LADAS*. However, Mahrt et al. (1996) have shown that averaging together our 10-min fluxes reduces the random error in our estimates, which more than offsets the slight loss of covariance under most wind conditions.

Figures 14 and 15 compare all the 30-min averaged flux estimates where there was at least 20 min of overlap. As one would expect, the comparisons show that the lateral components are smaller in magnitude than the longitudinal components except perhaps at low wind speeds. However, the absolute values of the R/V *Iselin* fluxes are generally larger than the R/P *LADAS*, and a correlation between the lateral component of the flux is not readily apparent. While some of the discrepancy could be caused by the underestimation of the fluxes from the R/P *LADAS* at low wind speeds, we believe that we have additional evidence that points to flow distortion as the primary cause for the disagreement.

d. Flow distortion

Because of its size, the catamaran is a much better wave follower than the ship. This causes the magnitude of the motion correction required for the R/P *LADAS* to be larger than the correction required for the R/V *Iselin*. Therefore, the reduced scatter and better agreement found in Fig. 11 versus Fig. 13 (as well as the smaller residual tilt) lead us to believe that most of the difference between the various flux comparisons is due to the effects of flow distortion on our ship-based measurements. This flow distortion is expected to influence both the mean flow and the turbulence. A comparison of the wind speeds relative to the ocean surface is shown in Fig. 16, where the *LADAS* winds have been brought up to 11.5 m using the friction velocity and stability corrections obtained from the bulk algorithm. While this

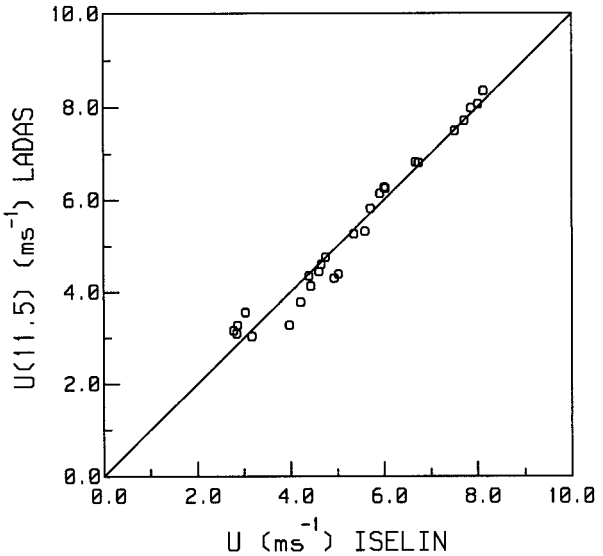

FIG. 16. A comparison of our relative wind speed measurements taken from the R/V *Iselin* and R/P *LADAS*. The R/P *LADAS* measurements have been adjusted to the height of the R/V *Iselin* measurements using the friction velocity and stability corrections computed using the bulk aerodynamic method of Fairall et al. (1996).

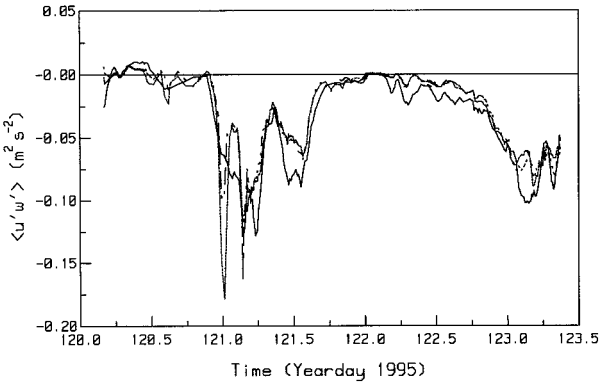

FIG. 17. A time series of the longitudinal component $\langle u'w' \rangle$ of the momentum flux measured aboard the R/P *FLIP* and R/V *Wecoma* during a 3-day period in May 1995. The dotted and dashed lines represent measurements taken at 8.7 and 13.8 m aboard the R/P *FLIP*, respectively. The solid line represents the R/V *Wecoma* data.

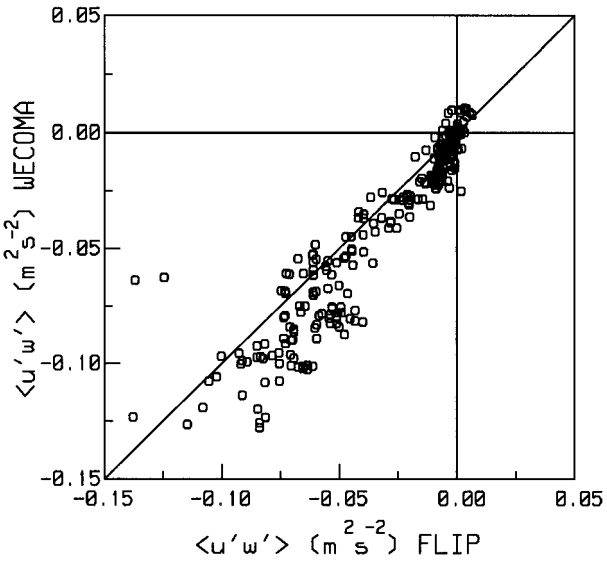

FIG. 18. A comparison of measurements of the longitudinal component $\langle u'w' \rangle$ of the momentum flux taken from the R/V *Wecoma* and R/P *FLIP*. The data represent 30-min averages computed when the R/V *Wecoma* was within 50 km of the R/P *FLIP*.

comparison exhibits some enhanced scatter at low wind speeds, any systematic difference between these velocity measurements is not readily apparent. As such, our suggestion that flow distortion causes the differences seen in the above figures remains speculative.

Fortunately, the MBL experiment provided us with the opportunity to compare our ship-based DCFS with the flux measurements made aboard the R/P *FLIP*. During the MBL experiment, the R/P *FLIP* was moored 40 km off the Monterey coast. A heavily instrumented 15-m mast was deployed at the end of the port boom by the first author and colleagues at the University of California, Irvine. This instrumentation was used to measure the momentum flux at three levels above the ocean surface. The velocity measurements from the *FLIP* also require motion correction before the fluxes were computed. However, because the corrections are typically an order of magnitude smaller than the ship-based system, we believe that this comparison provides a more quantitative evaluation of the DCFS.

Time series of the longitudinal component of the momentum flux measured at 8.7 m (dotted line) and 13.8 m (dashed line) aboard the R/P *FLIP* and at 11.3 m aboard the R/V *Wecoma* are shown in Fig. 17. This figure shows all of the flux estimates made when the ship was within 50 km of *FLIP* for relative wind directions between $-120°$ and $+120°$ of the bow. The time series shows that the fluxes follow each other very closely over the course of several frontal passages. However, this also indicates that the magnitude of the momentum fluxes from the ship are often higher than the R/P *FLIP*.

A direct comparison of these estimates is shown in Figs. 18 and 19, where the ship fluxes have been reduced by 15% in Fig. 19. The percentage was chosen based on a least squares fit to the data that gave a slope of 0.99 and intercept of -0.004. Correction of the R/V *Iselin* data by this same amount is shown in Fig. 20. The improved agreement in this figure provides further evidence, though indirect, that the bias is mainly due to flow distortion rather than inadequate motion correction.

We also attempted to quantify this increase as a function of relative wind direction. Unfortunately, there is not enough data to present a functional dependence of this increase on relative wind direction. However, it was clear that the magnitude of the required correction dramatically increased for directions beyond $\pm 130°$ of the bow. This is why we limited our comparisons to ± 120 in the comparisons shown in the above figures.

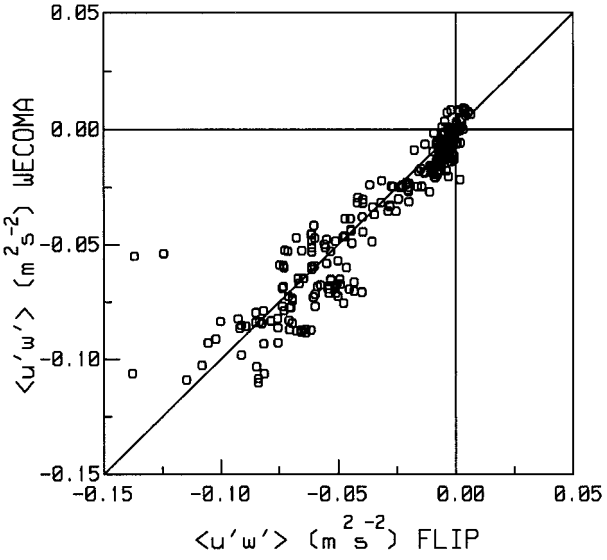

FIG. 19. As in Fig. 18 except that the R/V *Wecoma* estimates have been reduced by 15%.

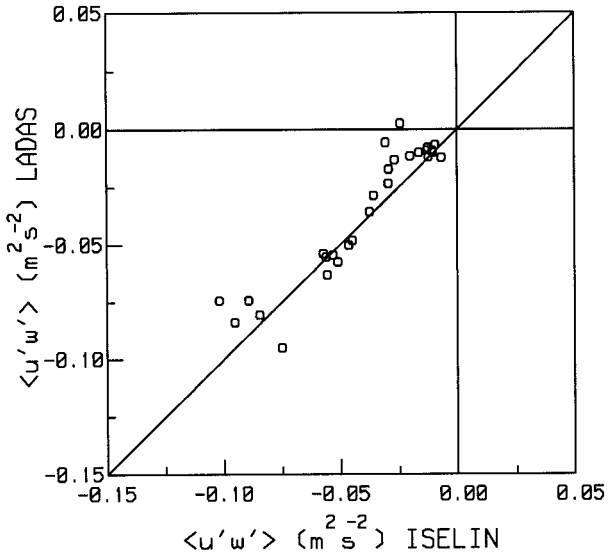

FIG. 20. As in Fig. 14 except that the R/V *Iselin* estimates have been reduced by 15%.

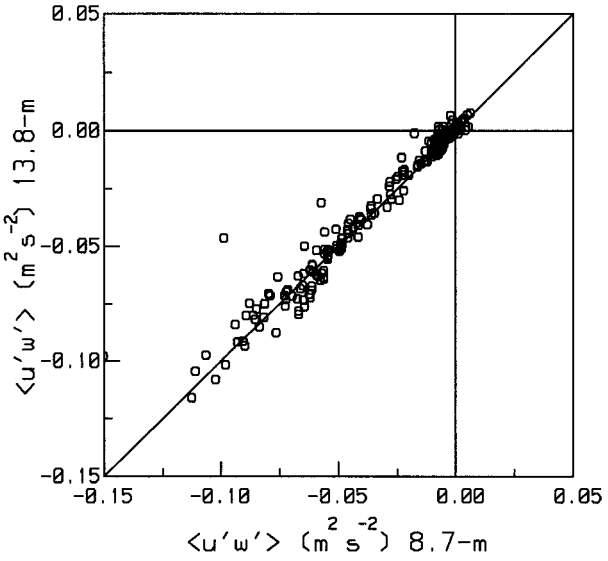

FIG. 21. A comparison of measurements of 30-min averaged longitudinal component $\langle u'w' \rangle$ of the momentum flux taken from the R/P *FLIP* at 8.7 and 13.8 m.

We believe that we have removed most of the bias in our flux estimates, reducing the flux by 15% and limiting our relative direction to within $\pm 120°$ of the bow. The scatter that remains in these figures is a combination of naturally occurring spatial variability and any remaining flow distortion or incomplete motion correction. The rms difference divided by the mean of these points gives an uncertainty of approximately 18% in Fig. 19. A comparison of the momentum flux estimates measured on *FLIP* at two different heights is shown in Fig. 21. If we assume that the differences between these two heights are due primarily to atmospheric variability, then at least 9% (as calculated above) of the *Wecoma* versus *FLIP* difference is due to this variability. In fact, it is very likely that more of the difference is due to horizontal variability, particularly because the surface temperature field was very inhomogeneous in the coastal ocean off Monterey.

Perhaps the most interesting comparison between the R/V *Wecoma* and R/P *FLIP* is shown in Fig. 22. Our previous comparisons have shown that the lateral component of the momentum stress is generally small enough so that it is difficult to distinguish between the signal and noise. However, in Fig. 22 we find strong evidence of a meteorological event that causes a noticeable lateral component in both the R/P *FLIP* and R/V *Wecoma* time series. During this period the ship was cruising toward the platform at approximately 2 kt. Rawinsonde launched from the ship indicated large wind shear in the upper boundary layer indicative of strongly baroclinic conditions. A frontal passage coinciding with the oscillation in the stress vector seen in this figure passed the platforms at different times as the ship steamed toward the R/P *FLIP*. We postulate that the decrease in the separation between the two platforms is responsible for the decreasing phase lag evident in the time series.

7. Conclusions

This paper has shown that the flux systems deployed in a number of recent over-sea field programs are capable of accurately measuring a direct estimate of the flux after removing the contamination in the signal due to platform motion and flow distortion. The ability to make these estimates from a research vessel is very advantageous since the mobility of a ship makes it a very effective platform for open-ocean measurements. Additionally, deployment from a ship allows us to make flux measurements under much worse conditions than possible with the catamaran.

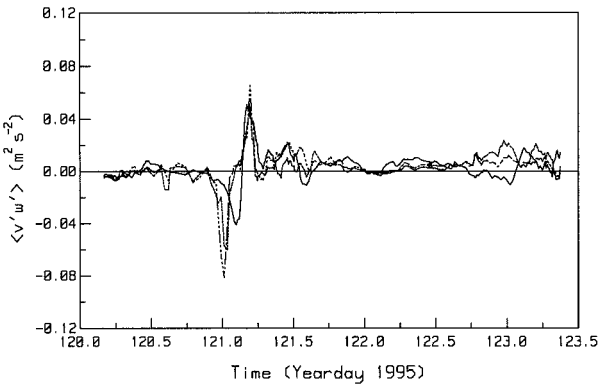

FIG. 22. A time series of the lateral component $\langle v'w' \rangle$ of the momentum flux measured aboard the R/P *FLIP* and R/V *Wecoma* during a 3-day period in May 1995. The dotted and dashed lines represent measurements taken at 8.7 and 13.8 m aboard the R/P *FLIP*, respectively. The solid line represents the R/V *Wecoma* data.

The comparisons shown in this paper indicate that the flow distortion causes an increase in the measured covariance of approximately 15% (or about 8% for the friction velocity). Though substantial, this correction is of a similar magnitude to the corrections for platform distortion applied to the HEXMAX dataset (Oost et al. 1994). Our evidence suggests that this correction is appropriate for the commonly used class of research vessels represented by the R/Vs *Wecoma* and *Iselin.* There is some evidence that this correction is a function of the direction of the relative wind vector. However, we do not have enough data processed from the R/P *FLIP* to make any definitive conclusions at this time.

Finally, some caution must be exercised when using ship-based measurements in studies examining the directional properties of marine surface layer turbulence (e.g., investigations of the influence of misaligned wind and waves on the stress vector). This caution is necessary because of the magnitude of the flow distortion and motion contamination relative to the magnitude of the lateral component of the flux. However, it appears that the fluxes can be used in case studies of directional processes under conditions where the cross-stream component of the vector stress is comparable with the along-wind component, as shown in Fig. 22. Additionally, many problems associated with flow distortion can be circumvented through use of smaller coastal vessels, low-profile towed vehicles, and moored platforms such as the R/P *LADAS,* surface buoys (e.g., Anctil et al. 1994), and the R/P *FLIP*. In fact, the time series showing the lateral component of the stress vector points out one advantage of having both mobile and moored platforms in studies investigating air–sea interactions.

Acknowledgments. The authors would like to thank Erik Bock and Fredrik Thwaites for their helpful discussions during the construction of both the system and processing algorithms, and Ditmar Bock for his suggestions on the use of complementary filtering. The engineering, technical, and scientific contributions of Nick Witzell, David Schroeder, Steve Murphy, Robert Handy, and John Boutillette at WHOI and Dave Gregg, Scott Abbott, Jesse Leach, Cat Russell, and Norbert Szczepczynski at NOAA/ETL are also acknowledged. The first author would like to thank Judy White for her assistance in preparing the manuscript. Special thanks go to Scott Miller and Carl Friehe of UC-Irvine for their help in collecting and processing the R/P *FLIP* data. The High Resolution and MBL components of this research has been supported by the Office of Naval Research (Grants N00014-92-J-1585, N00014-93-1-0274, and N00014-96-1-0012). Partial support for the NOAA/ETL component has been provided by the DOE Atmospheric Radiation Measurement program and the U.S. National Oceanic and Atmospheric Administration Climate and Global Change Program.

REFERENCES

Anctil, F., M. A. Donelan, W. M. Drennan, and H. C. Graber, 1994: Eddy-correlation measurements of air–sea fluxes from a discus buoy. *J. Atmos. Oceanic Technol.,* **11,** 1144–1150.

Anderson, R. J., 1993: A study of wind stress and heat flux over the open ocean by the inertial-dissipation method. *J. Phys. Oceanogr.,* **23,** 2153–2161.

Axford, D. N., 1968: On the accuracy of wind measurements using an inertial platform in an aircraft and an example of a measurement of the vertical mesostructure of the atmosphere. *J. Appl. Meteor.,* **7,** 645–666.

Bock, E. J., and T. Hara, 1995: Optical measurements of capillary–gravity wave spectra using a scanning laser slope gauge. *J. Atmos. Oceanic Technol.,* **12,** 395–403.

Davidson, K. L., C. E. Skupniewicz, D. Ross, R. G. Onstott, J. A. Johannessen, and O. Skagseth, 1991: Relationship between wind stress, backscatter, and the directional wave spectrum. *Proc. OCEANS '91,* Honolulu, HI, IEEE, 998–1005.

Dugan, J. P., S. L. Panichas, and R. L. DiMarco, 1991: Decontamination of wind measurements from buoys subject to motions in a seaway. *J. Atmos. Oceanic Technol.,* **8,** 85–95.

Edson, J. B., C. W. Fairall, S. E. Larsen, and P. G. Mestayer, 1991: A study of the inertial-dissipation technique for computing air-sea fluxes. *J. Geophys. Res.,* **96,** 10 689–10 711.

Fairall, C. W., and S. E. Larsen, 1986: Inertial dissipation methods and turbulent fluxes at the air ocean interface. *Bound.-Layer Meteor.,* **34,** 287–301.

——, and G. S. Young, 1991: A field evaluation of shipboard performance of an infrared hygrometer. Preprints, *Seventh Symp. on Meteorological Observations and Measurements,* New Orleans, LA, Amer. Meteor. Soc., 311–315.

——, ——, S. E. Larsen, and P. G. Mestayer, 1990: Inertial-dissipation air–sea flux measurements: A prototype system using real-time spectral computations. *J. Atmos. Oceanic Technol.,* **7,** 425–453.

——, E. F. Bradley, D. P. Rogers, J. B. Edson, and G. S. Young, 1996: Bulk parameterization of air-sea fluxes for TOGA COARE. *J. Geophys. Res.,* **101,** 3747–3764.

——, A. B. White, J. B. Edson, and J. E. Hare, 1997: Integrated shipboard measurements of the marine boundary layer. *J. Atmos. Oceanic Technol.,* **14,** 368–379.

Friehe, C. A., J. C. LaRue, F. H. Champagne, C. H. Gibson, and G. F. Dreyer, 1975: Effect of temperature and humidity fluctuations on the optical refractive index in the marine boundary layer. *J. Opt. Soc. Amer.,* **65,** 1502–1511.

Fujitani, T., 1981: Direct measurement of turbulent fluxes over the sea during AMTEX. *Pap. Meteor. Geophys.,* **32,** 119–134.

——, 1985: Method of turbulent flux measurement on a ship by using a stable platform system. *Pap. Meteor. Geophys.,* **36,** 157–170.

Geernaert, G. L., 1988: Measurements of the angle between the wind vector and wind stress vector in the surface layer over the North Sea. *J. Geophys. Res.,* **93,** 8215–8220.

——, F. Hansen, M. Courtney, and T. Herbers, 1993: Directional attributes of the ocean surface wind stress vector. *J. Geophys. Res.,* **98,** 16 571–16 582.

Goldstein, H., 1965: *Classical Mechanics.* Addison-Wesley, 398 pp.

Hamming, R. W., 1977: *Digital Filters.* Prentice-Hall, 297 pp.

Hare, J. E., J. B. Edson, E. J. Bock, and C. W. Fairall, 1992: Progress on direct covariance measurements of air-sea fluxes from ships and buoys. Preprints, *10th Symp. Turbulence and Diffusion,* Portland, OR, Amer. Meteor. Soc., 281–284.

Herr, F., C. Luther, G. Marmorino, R. Mied, and D. Thompson, 1991: Ocean surface remote sensing program planned. *Eos, Trans. Amer. Geophys. Union,* **72,** 214.

Kaimal, J. C., J. C. Wyngaard, Y. Izumi, and O. R. Cote, 1972: Spectral characteristics of surface layer turbulence. *Quart. J. Roy. Meteor. Soc.,* **98,** 563–589.

Large, W. G., and S. Pond, 1981: Open ocean momentum flux mea-

surements in moderate to strong winds. *J. Phys. Oceanogr.*, **11,** 324–336.

——, and ——, 1982: Sensible and latent heat flux measurements over the ocean. *J. Phys. Oceanogr.*, **12,** 464–482.

Larsen, S. E., J. B. Edson, C. W. Fairall, and P. G. Mestayer, 1993: Measurement of temperature spectra by a sonic anemometer. *J. Atmos. Oceanic Technol.*, **10,** 345–354.

Lenschow, D. H., and P. Spyers-Duran, 1987: Measurement techniques: Air motion sensing. NCAR Bulletin 23, 361 pp. [Available from National Center for Atmospheric Research, P.O. Box 3000, Boulder, CO 80303.]

Liu, W. T., K. B. Katsaros, and J. A. Businger, 1979: Bulk parameterizations of the air–sea exchange of heat and water vapor including the molecular constraints at the interface. *J. Atmos. Sci.*, **36,** 1722–1735.

Oost, W. A., C. W. Fairall, J. B. Edson, S. D. Smith, R. J. Anderson, J. A. B. Wills, K. B. Katsaros, and J. DeCosmo, 1994: Flow distortion calculations and their application in HEXMAX. *J. Atmos. Oceanic Technol.*, **11,** 366–386.

Rieder, K. F., J. A. Smith, and R. A. Weller, 1994: Observed directional characteristics of the wind, wind stress, and surface waves on the open ocean. *J. Geophys. Res.*, **99,** 22 589–22 596.

Smith, S. D., 1988: Coefficients for sea surface wind stress, heat flux and wind profiles as a function of wind speed and temperature. *J. Geophys. Res.*, **93,** 15 467–15 472.

Twaites, F. T., 1995: Development of an acoustic vorticity meter to measure shear in ocean-boundary layers. Ph.D. thesis, Massachusetts Institute of Technology and Woods Hole Oceanographic Institution, 186 pp.

Yelland, M. J., P. K. Taylor, I. E. Consterdine, and M. H. Smith, 1994: The use of the inertial dissipation technique for shipboard wind stress determination. *J. Atmos. Oceanic Technol.*, **11,** 1093–1108.